

ELECTRONIC SUPPLEMENTARY INFORMATION

A Synthetic Model of the Nonheme Iron-Superoxo Intermediate of Cysteine Dioxygenase

Anne A. Fischer, Sergey V. Lindeman and Adam T. Fiedler*

EXPERIMENTAL SECTION

General materials: All reagents and solvents were purchased from commercial sources and used as received unless otherwise noted. Acetonitrile and dichloromethane were purified and dried using a Vacuum Atmospheres solvent purification system. The synthesis and handling of air-sensitive materials were carried out under an inert atmosphere using a Vacuum Atmospheres Omni-Lab glovebox. $[\text{Fe}(\text{OAc})(\text{Tp}^{\text{Me}_2})]$ was prepared using a previously-published procedure.¹

Physical and spectroscopic methods: Elemental analysis results were obtained from Midwest MicroLab, LLC in Indianapolis, IN. Infrared (IR) spectra of solid samples were measured with a Thermo Scientific Nicolet iS5 FTIR spectrometer equipped with the iD3 attenuated total reflectance accessory. UV-vis absorption spectra were collected with an Agilent 8453 diode array spectrometer equipped with a Unisoku Scientific Instruments (Osaka, Japan) cryostat for low temperature measurements. ¹H NMR spectra were measured on a Varian 400 MHz spectrometer. X-band EPR spectra were measured using a Bruker EMXplus instrument. Magnetic circular dichroism (MCD) data were collected by placing the sample in an Oxford Instrument SM-4000 8T magnetocryostat. Spectra were measured using a Jasco Model J-715 spectropolarimeter, and the -7 T spectrum was subtracted from the +7 T spectrum to eliminate artifacts.

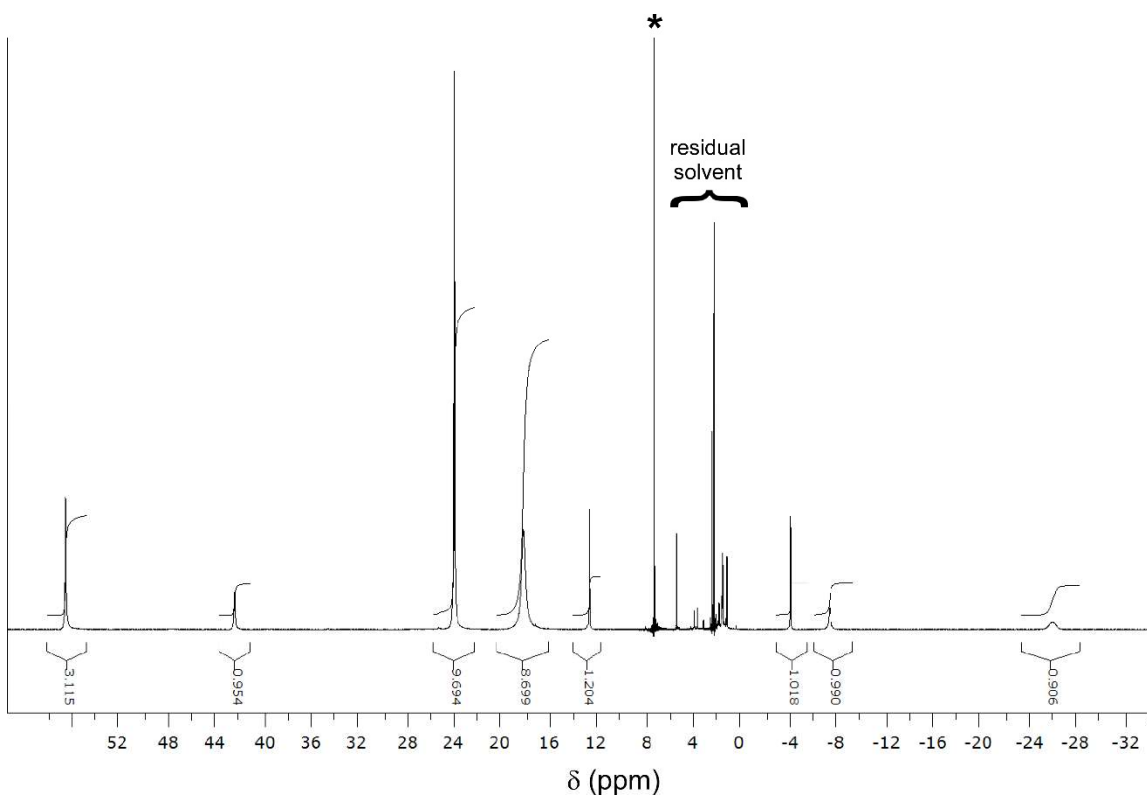
Resonance Raman (rRaman) samples of **2** were generated from solutions of **1** in THF, THF-d₈, or MeTHF with concentrations ranging from 8 to 13 mM. These solutions were added to NMR tubes in a glovebox, frozen in liquid nitrogen, and attached to a Schlenk line while frozen. After performing three vacuum/argon cycles, the samples were exposed to gaseous dioxygen (¹⁶O₂ or ¹⁸O₂) and allowed to warm to -78 °C using a dry ice/acetone bath. The solutions developed the dark purple color of **2** upon melting, and the fully liquid solutions were mixed with a Vortex stirrer. Approximately 30 seconds after melting, the samples of **2** were refrozen in liquid N₂ and detached

from the Schlenk line. The rRaman data were measured using 501.7 nm excitation from a Coherent I-305 Ar⁺ laser (~40 mW of power at the sample). The light scattered from the frozen samples (77 K) was collected using a 135° backscattering arrangement and dispersed by an Acton Research triple monochromator featuring a 1200 grooves/mm grating. The scattered light was detected with a Princeton Instruments Spec X 100BR deep depletion, back-thinned CCD camera. Peak frequencies were calibrated with reference to K₂SO₄ and solvent peaks.

Synthesis of [Fe(Tp^{Me2})(2-ATP)] (1): Two different procedures were used to prepare complex **1**. *Procedure A:* The 2-aminothiophenol pro-ligand (0.125 g, 1.0 mmol) was combined with a slight excess of NaOMe (0.060 g, 1.1 mmol) in THF (3 mL). After stirring for 30 minutes, the solvent was removed under vacuum to yield a white solid. To this flask was added equimolar amounts of Fe(OTf)₂ (0.35 g, 1.0 mmol) and K(Tp^{Me2}) (0.34 g, 1.0 mmol) in MeCN (8 mL). The resulting mixture was stirred for 12 hours, followed by filtration through Celite to remove unwanted byproducts, namely Fe(Tp^{Me2})₂ and inorganic salts. The filtrate was dried under vacuum to yield the crude product as a yellow solid. Recrystallization from a CH₂Cl₂/hexane solution cooled to -10 °C provided complex **1** as a microcrystalline solid. Although this procedure yielded pure material, yields were low (~ 10%) due to the unavoidable formation of Fe(Tp^{Me2})₂. We therefore pursued an alternative route to **1** that employed a precursor complex, [Fe(Tp^{Me2})(OAc)], used by Hikichi *et al.* to generate a related Tp^{Me2}-based iron(II) complex.¹ *Procedure B:* 2-aminothiophenol (0.125 g, 1.0 mmol) was treated with excess of NaOMe (0.162 g, 3.0 mmol) in THF (5 mL) and stirred for 30 minutes. The volatiles were removed by vacuum and the remaining residue was taken up in CH₃CN (3 mL). This solution was slowly combined with a separate solution of [Fe^{(Me2)Tp}(OAc)] (0.135 g, 0.33 mmol) dissolved in CH₃CN (3 mL). The resulting mixture was stirred for two hours, followed by removal of solvent *en vacuo*. The solid was taken up in CH₂Cl₂ and filtered through Celite. After evaporation of solvent, the residue was redissolved in CH₃CN, filtered again through Celite, and dried under vacuum to yield a yellow solid. Residual 2-aminothiophenol was removed by repeated washes with diethyl ether, followed by recrystallization from CH₂Cl₂/hexane at -10 °C. Yield = 51 mg (32%) The spectroscopic properties and O₂ reactivity of complex **1** were independent of the manner of preparation.

Anal. Calcd for C₂₁H₂₈BF₂FeN₇S·CH₂Cl₂ (*MW* = 562.15 g mol⁻¹): C, 47.00; H, 5.38; N, 17.44. Found: C, 46.87; H, 5.36; N, 17.95. UV-vis [λ_{\max} , nm (ϵ , M⁻¹cm⁻¹) in THF]: 558 (125), 917 (90). FTIR (cm⁻¹, solid): 3345 [ν (N-H)], 2546 [ν (B-H)], 1543, 1384. ¹H NMR (400 MHz, CDCl₃): δ

= 56.7 (s, 3H, 4-*H*-pz), 42.5 (s, 1H, B-*H*), 24.0 (s, 9H, 5-Me-Tp), 18.2 (s, 9H, 3-Me-Tp), 12.7 (s, 1H, 2-ATP), -4.18 (s, 1H, 2-ATP), -7.47 (s, 1H, 2-ATP), -26.2 (s, 1H, 2-ATP). The ^1H NMR spectrum of **1** is shown below:



^1H NMR spectrum of **1** in CDCl_3 at room temperature. The CHCl_3 peak is labeled with an asterisk (*) and peaks due to residual solvent (CH_2Cl_2 and hexane) are also indicated. The presence of paramagnetically-shifted peaks between 60 and -30 ppm is typical of high-spin Fe(II) complexes. Based on integrations, the peak at 57 ppm (3H) is attributed to the 4-pyrazole protons, while those at 24 and 18 ppm are assigned to the 5-Me and 3-Me substituents pyrazole substituents, respectively. The H-B resonance (1H) appears at 42 ppm. A similar pattern of Tp^{Me2}-derived peaks was observed for $[\text{Fe}(\text{OAc})(\text{Me}_2\text{Tp})]$.¹ The aromatic 2-ATP protons are evident at 13, -4.2, -7.5, and -26 ppm (1H each).

Analysis of O₂ Reaction Products. Following established procedures,^{2,3} O₂ gas was bubbled through a solution of **1** (0.040 g) in THF at room temperature and allowed to stir for 12 hours. The THF was removed *en vacuo* and the remaining residue was taken up in CH_2Cl_2 . After addition of 3 M HCl (6 mL), the mixture was stirred for 3 hours. The aqueous layer was collected and the dried under vacuum. The resulting residue was taken up in CH_3OH and Chelex (50-100 mesh) was added, and this mixture was stirred for 12 hours. After filtration, the solvent was removed under vacuum and the residue was washed with toluene to remove free pyrazole. Final drying

provided 5.4 mg of the disulfide product (52% yield). ^1H NMR data of the reaction products, shown in Figure S6, were interpreted with the aid of published spectra obtained with commercially available material.

X-ray Crystallography: X-ray quality crystals of **1** were grown by dissolving the complex in a minimal amount of CH_3CN and allowing the solvent to slowly evaporate. Diffraction data were collected at 100 K with an Oxford Diffraction SuperNova kappa-diffractometer (Rigaku Corp.) equipped with dual Cu/Mo X-ray sources, X-ray mirror optics, an Atlas CCD detector, and a low-temperature Cryojet device. The data were analyzed with the CrysAlis(Pro) program package, followed by numerical absorption correction based on Gaussian integration over a multifaceted crystal model. The empirical absorption correction, using spherical harmonics, was implemented in the SCALE3 ABSPACK scaling algorithm. Structures were solved using the SHELXS program and refined with the SHELXL program⁴ as part of the Olex2 crystallographic package.⁵ X-ray diffraction parameters are summarized below; CCDC 1851803 contains the supplementary crystallographic data (CIF file) for complex **1**. This file can be obtained from the Cambridge Crystallographic Data Centre via the following website: www.ccdc.cam.ac.uk/data_request/cif.

Crystallographic data for **1**: $\text{C}_{21}\text{H}_{28}\text{BFeN}_7\text{S}$, $M_r = 477.22 \text{ g mol}^{-1}$, orthorhombic, space group $Pbca$, $a = 15.19917(12)$, $b = 13.84434(12)$, $c = 21.58924(15) \text{ \AA}$, $\alpha = 90.00$, $\beta = 90.00$, $\gamma = 90.00^\circ$, $V = 4542.86(6) \text{ \AA}^3$, $Z = 8$, $\rho = 1.396 \text{ g cm}^{-3}$, reflections collected 39263, independent reflections 4345 ($R_{\text{int}} = 0.0292$), 294 parameters, $R_1 = 0.0245$ for $I \geq 2\sigma(I)$ and $wR_2 = 0.0629$.

Table S1. Selected Bond Distances (Å) and Bond Angles (deg) Derived from the X-ray Crystal Structure of Complex **1**.

<i>Bond Distances</i>		<i>Bond Angles</i>	
Fe1–S1	2.3107(4)	S1–Fe1–N2	121.83(3)
Fe1–N2	2.0746(12)	S1–Fe1–N4	140.45(4)
Fe1–N4	2.0817(12)	S1–Fe1–N6	105.19(3)
Fe1–N6	2.1843(12)	S1–Fe1–N7	82.86(3)
Fe1–N7	2.2776(13)	N2–Fe1–N4	97.04(5)
S1–C16	1.7660(15)	N2–Fe1–N6	85.50(4)
N7–C17	1.4509(17)	N2–Fe1–N7	91.79(5)
		N4–Fe1–N6	83.16(4)
		N4–Fe1–N7	89.45(5)
		N6–Fe1–N7	171.75(5)

Density Functional Theory (DFT) Calculations

General Methodology. DFT calculations of **2** were performed with the ORCA 3.0 software package developed by Dr. F. Neese (MPI for Chemical Energy Conversion).⁶ The computational model was constructed by addition of O₂ to the crystallographic structure of **1**, followed by geometry optimization. The Tp^{Me2} supporting ligand was modified by replacing the 5-methyl substituents with hydrogen atoms. Optimized structures correspond to local energy minima with only real vibrational frequencies. The calculations employed Ahlrichs' valence triple- ζ basis set (TZV) and polarization functions on main-group and transition-metal elements (default-basis 3 in ORCA).⁷⁻⁹ Two different functionals were utilized: (i) Becke's three-parameter hybrid functional for exchange along with the Lee-Yang-Parr correlation functional (B3LYP),^{10, 11} and (ii) the meta-generalized gradient approximation (meta-GGA) TPSS functional.¹² Computational costs were reduced by applying the resolution of identity and chain of sphere (RIJCOSX) approximation¹³ and the TZV/J auxiliary basis set.¹⁴ Broken-symmetry wavefunctions, such as the $S_{\text{tot}} = 2$ and 1 states of **2**, were achieved using the "spin-flip" feature of ORCA. Transition-state geometries were located by performing a relaxed surface scan along the bond being formed, and the existence of the transition state was confirmed by an imaginary vibration along the bond-forming mode. Frequency calculations provided zero-point energies, thermal corrections, and entropy terms (vibrational, rotational, and translational), which were used to compute the Gibbs free energy ($G = H - TS$) at 298 K for each model.

Time-dependent DFT (TD-DFT) calculations employed the cam-B3LYP range-separated hybrid functional,¹⁶ which has been shown to provide excellent agreement between experimental and computed absorption spectra for CDO and related model complexes.^{17, 18} Absorption energies and intensities were computed for 40 excited states using the Tamm-Dancoff approximation.^{19, 20} The nature of computed transitions was determined through analysis of electron-density difference maps (EDDMs) visualized using the *ChemCraft* program.

Computational Models of **2 in Different Spin States.** Due to exchange interactions between the unpaired electrons of Fe and O₂, four spin-states are possible for **2**: singlet ($S = 0$), triplet ($S = 1$), quintet ($S = 2$), or septet ($S = 3$). The $S = 0$ possibility was not considered because MCD studies indicate that **2** is paramagnetic. The septet and quintet states arise from ferromagnetic and antiferromagnetic coupling, respectively, between a high-spin (HS) Fe(III) center and superoxo radical. The triplet state emerges from either (i) antiferromagnetic coupling between a high-spin Fe(II) center and neutral O₂ ligand or (ii) ferromagnetic coupling between a low-spin Fe(III) ion and O₂^{•-} radical. We therefore considered four computational models of **2** for each functional. These models are labeled ^{spin}[**2**]^(HS,LS), where HS and LS indicate whether the Fe center is high-spin or low-spin, respectively. Table S2 summarizes the relative energies and computed $\nu(\text{O-O})$ frequencies for models generated using the hybrid B3LYP and meta-GGA TPSS functionals. Geometry optimizations of ^{S=3}[**2**]^{HS} and ^{S=1}[**2**]^{HS} performed with the B3LYP functional failed to converge due to dissociation of the O₂ ligand from the Fe center. In all other cases, the superoxide ligand adopts a bent conformation (Fe-O-O angle between 120 and 128°) that allows it to form a hydrogen bond with the -NH₂ donor of 2-ATP.

Table S2. DFT-Computed Energies and $\nu(\text{O-O})$ Frequencies for **2**

Functional	S_{tot} (Fe spin) ^a	Relative E (kcal/mol)	$\nu(\text{O-O})$ (cm^{-1})
B3LYP	$S = 3$ (HS)	n.a. ^b	n.a.
	$S = 2$ (HS)	0.0	1156
	$S = 1$ (HS)	n.a.	n.a.
	$S = 1$ (LS)	4.0	1163
TPSS	$S = 3$ (HS)	15.0	1128
	$S = 2$ (HS)	12.8	1186
	$S = 1$ (HS)	13.9	1196
	$S = 1$ (LS)	0.0	1086

^a S_{tot} is the overall spin of **2** and HS/LS indicate the spin state of the Fe center.

^b n.a. = data not available because the geometry optimization failed to converge to a O_2 -bound structure; instead, the O_2 ligand dissociates to yield a five-coordinate Fe(II) complex.

The quintet spin-state provides lowest-energy model of **2** in the B3LYP calculations, whereas the triplet model with a low-spin Fe center, $S=1[\mathbf{2}]^{\text{LS}}$, is the ground state in the TPSS calculations. This scenario is consistent with the well-established propensity of hybrid functionals to favor high-spin configurations, while non-hybrid functionals tend to stabilize low-spin configurations. Due to the discrepancy between functionals, it is not possible to determine the spin-state of **2** based on energetics alone. The computed $\nu(\text{O-O})$ frequencies are also inadequate for discriminating between the various models. We therefore turned to time-dependent DFT (TD-DFT) calculations to determine which model best reproduces the distinctive UV-vis absorption features of **2**. Figure S5 compares the experimental absorption spectrum to those computed by TD-DFT using the cam-B3LYP functional. It is clear from this figure that the computed $S = 2$ spectrum nicely mimics the salient features of the experimental spectrum, whereas the $S = 1$ (LS) spectrum deviates greatly from the experimental data. The $S = 1$ (LS) spectrum exhibits a single intense band at 550 nm arising from a $S \rightarrow \text{Fe(III)}$ charge transfer (CT) transition, and it lacks features with $\lambda_{\text{max}} > 600$ nm. In contrast, the $S = 2$ spectrum consists of multiple features across the visible region and reproduces the presence of bands at longer wavelengths (600 - 900 nm). The features in the computed spectra are assigned according to the dominant contributor to the electronic transition (Figure S5).

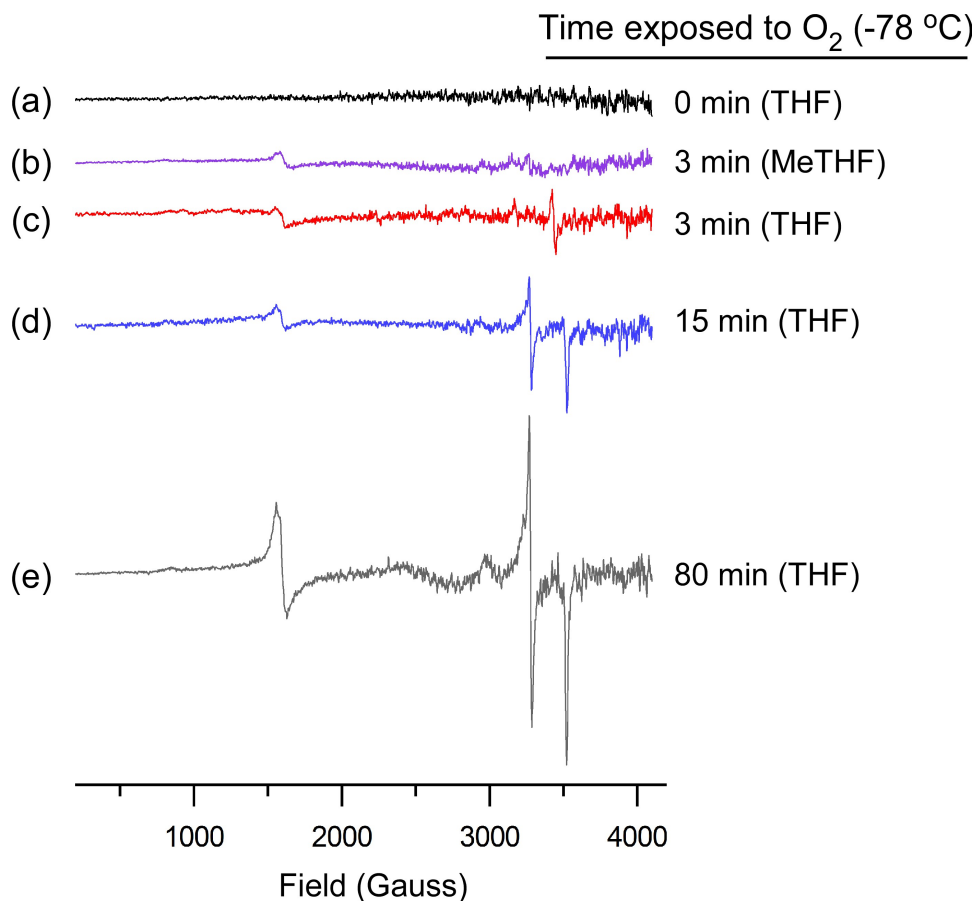


Figure S1. Time-dependent X-band EPR spectral changes during the reaction of **1** (1.7 mM) with O₂ at -78 °C in THF or MeTHF. No signal is observed for the anaerobic sample of **1** (a). Samples of **2** in MeTHF (b) or THF (c) were generated by exposure of **1** to O₂ for 3 minutes, which ensures complete formation of **2**. These spectra are nearly featureless due to the EPR-silent nature of **2**. The weak features at $g \sim 2.0$ and 4.3 are due to the EPR-active decay product (**3**). The decay features gain intensity with time, as revealed by spectra of samples exposed to O₂ for 15 min (d) and 80 min (e). All spectra were measured using the same parameters: frequency = 9.62 GHz; temperature = 77 K; microwave power = 2 mW; modulation amplitude = 10 G; time constant = 0.04 s; receiver gain = 60 dB.

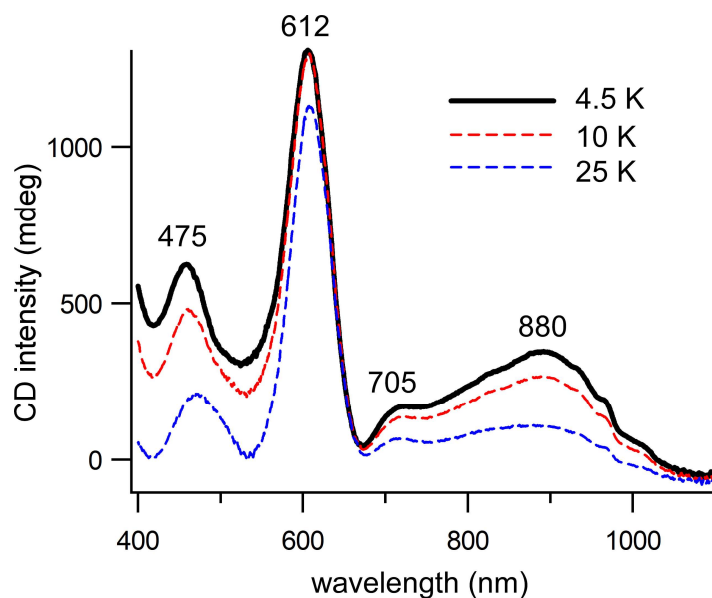


Figure S2. Variable-temperature MCD spectra of **2** (2.9 mM) in MeTHF glass. Spectra were collected at a magnetic field of 7 T and temperatures of 4.5, 10, and 25 K.

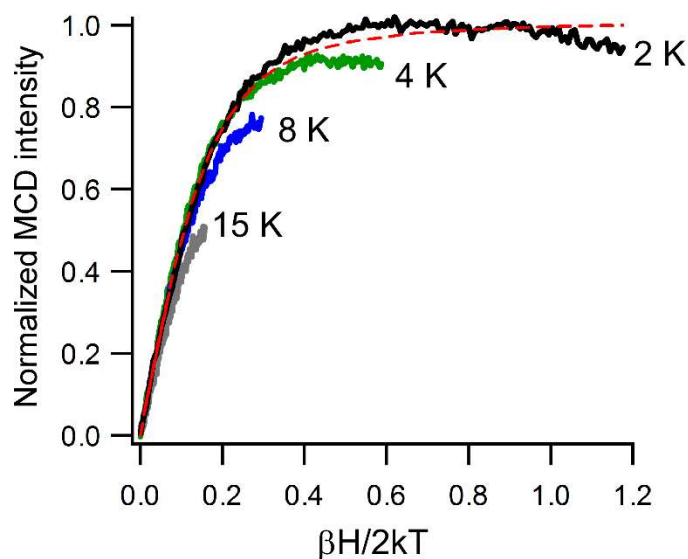


Figure S3. Variable-temperature variable-field MCD data measured at 885 nm for **2** (2.9 mM) in MeTHF glass. Data were collected at the indicated temperatures by scanning the magnetic field (H) from 0 to 7 T. By convention, the normalized MCD intensity is plotted versus $\beta H / 2kT$. The red dashed line is the theoretical magnetization curve for an axial $S = 2$ compound ($g_{\parallel} = 8.0$ and $g_{\perp} = 0.0$; xy -polarized transition).

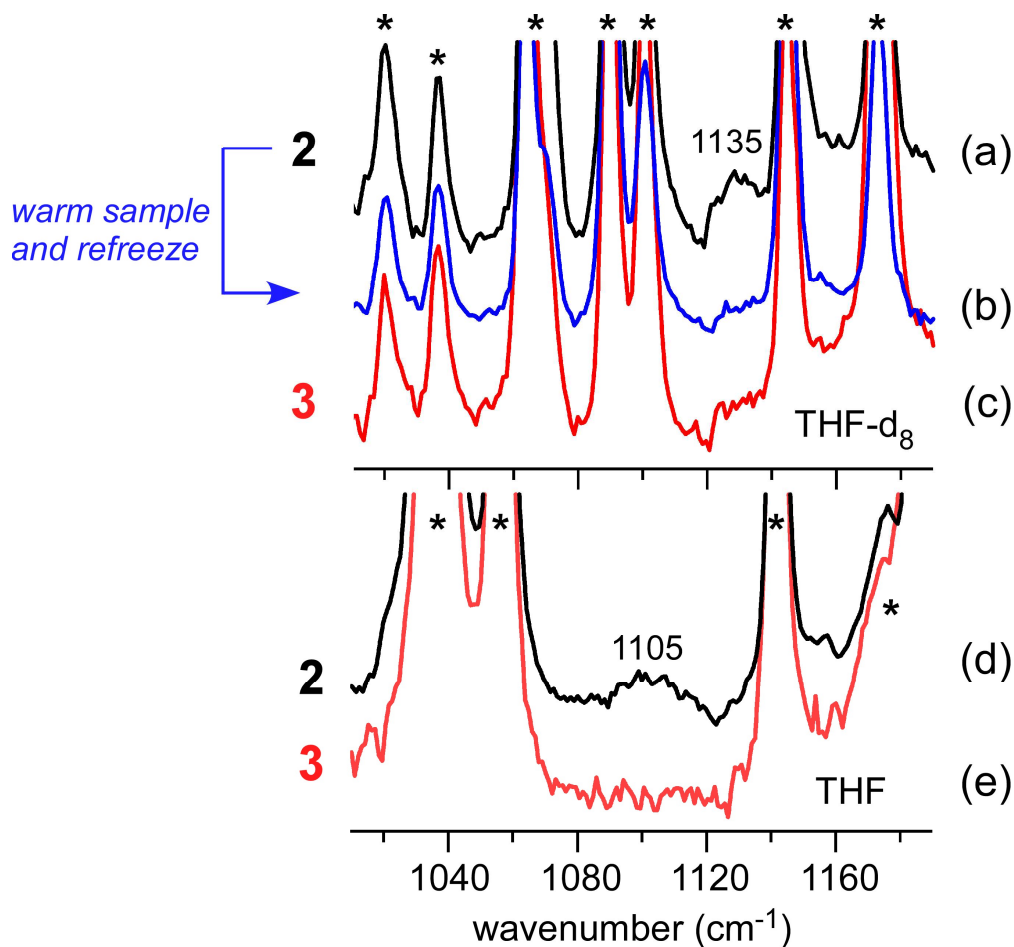


Figure S4. *Top spectra (a-c, THF-d₈ solvent):* (a) The rRaman spectrum of **2**, (b) the spectrum collected after warming and refreezing the sample, revealing loss of the peak at 1135 cm⁻¹, and (c) the spectrum of **3** prepared by exposing a solution of **1** to O₂ at room temperature. *Bottom spectra (d-e, THF solvent):* Comparison of the rRaman spectra measured for **2** (d) and **3** (e) in frozen THF, where **3** was generated in the same manner as sample (c). Data were gathered using 501.7 nm laser excitation (40 mW); peaks marked with an asterisk (*) are due to solvent.

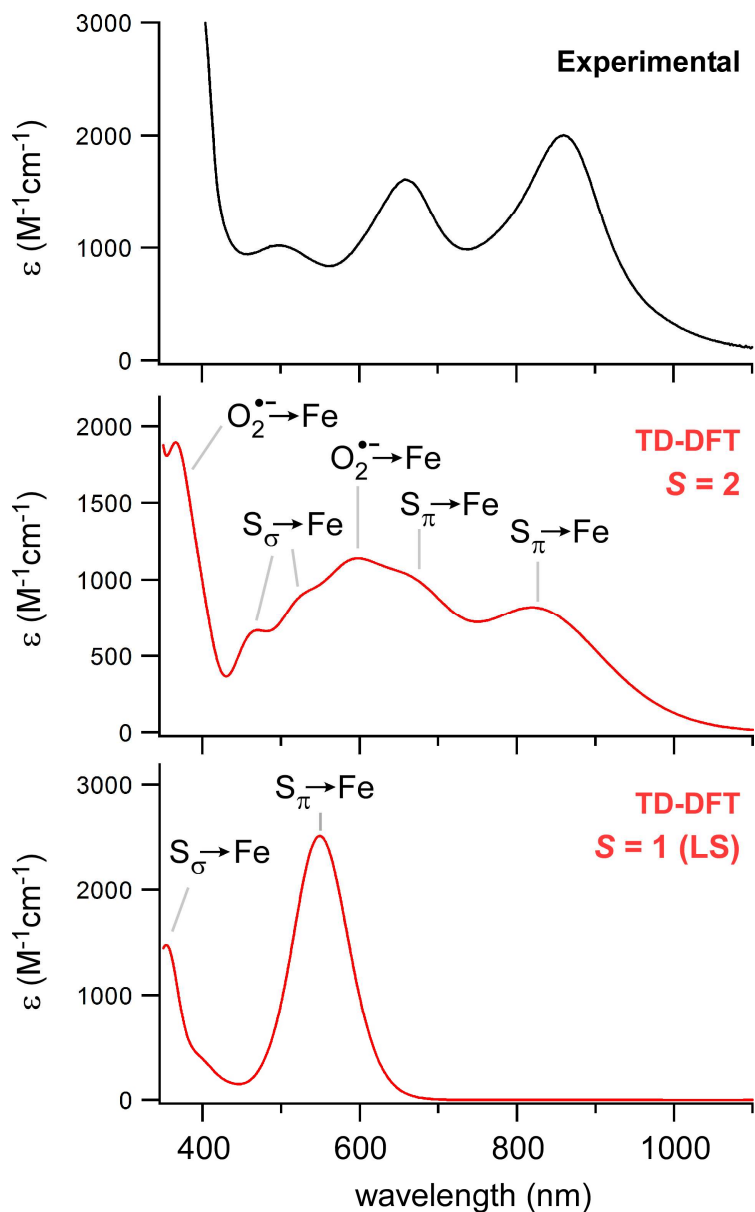


Figure S5. Comparison of experimental and TD-DFT absorption spectra. *Top:* Experimental UV-vis absorption spectrum of **2** at $-80\text{ }^{\circ}\text{C}$ in THF. *Middle:* TD-DFT computed absorption spectrum of **2** in the quintet ($S = 2$) state (i.e., high-spin Fe(III) center antiferromagnetically-coupled to a superoxide radical). *Bottom:* TD-DFT computed absorption spectrum of **2** in the triplet ($S = 1$) state (i.e., low-spin Fe(III) center ferromagnetically coupled to a superoxide radical). The lines point to features in the computed spectra arising from the indicated type of electronic transition.

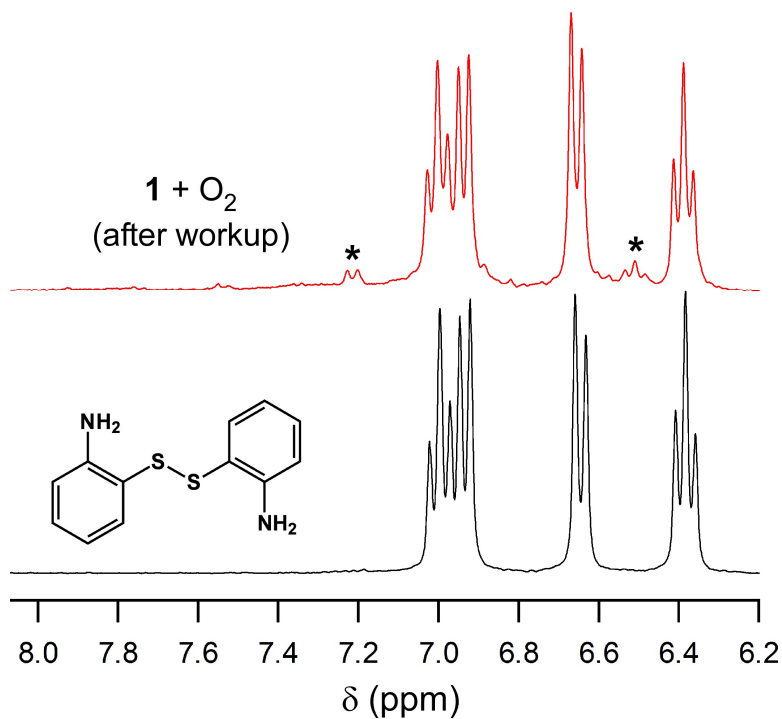


Figure S6. Comparison of the ¹H NMR spectrum of the isolated product of O₂ oxidation (top, red line) to the spectrum of 2-aminophenyl disulfide (bottom, black line) prepared using commercial-available compound. Both spectra were measured in MeOH-*d*₄ solvent. The features indicated by asterisks (*) arise from residual 2-aminothiophenol.

REFERENCES

1. F. Oddon, Y. Chiba, J. Nakazawa, T. Ohta, T. Ogura and S. Hikichi, *Angew. Chem. Int. Ed.*, 2015, **54**, 7336-7339.
2. M. Sallmann, B. Braun and C. Limberg, *Chem. Commun.*, 2015, **51**, 6785-6787.
3. M. Sallmann, I. Siewert, L. Fohlmeister, C. Limberg and C. Knispel, *Angew. Chem. Int. Ed.*, 2012, **51**, 2234-2237.
4. G. M. Sheldrick, *Acta Crystallogr. Sect. A*, 2008, **64**, 112-122.
5. O. V. Dolomanov, L. J. Bourhis, R. J. Gildea, J. A. K. Howard and H. Puschmann, *J. Appl. Crystallogr.*, 2009, **42**, 339-341.
6. F. Neese. ORCA - An Ab Initio, DFT and Semiempirical Electronic Structure Package, version 3.0, Max Planck Institute for Chemical Energy Conversion, Muelheim (Germany), 2013.
7. A. Schafer, C. Huber and R. Ahlrichs, *J. Chem. Phys.*, 1994, **100**, 5829-5835.
8. A. Schafer, H. Horn and R. Ahlrichs, *J. Chem. Phys.*, 1992, **97**, 2571-2577.
9. F. Weigend and R. Ahlrichs, *Phys. Chem. Chem. Phys.*, 2005, **7**, 3297-3305.
10. A. D. Becke, *J. Chem. Phys.*, 1993, **98**, 5648-5652.
11. C. T. Lee, W. T. Yang and R. G. Parr, *Physical Review B*, 1988, **37**, 785-789.
12. J. Tao, J. P. Perdew, V. N. Staroverov and G. E. Scuseria, *Phys. Rev. Lett.*, 2003, **91**, 146401-146404.
13. F. Neese, F. Wennmohs, A. Hansen and U. Becker, *Chem. Phys.*, 2009, **356**, 98-109.
14. K. Eichkorn, O. Treutler, H. Oehm, M. Haeser and R. Ahlrichs, *Chem. Phys. Lett.*, 1995, **240**, 283-290.
15. A. Klamt and G. Schueuermann, *J. Chem. Soc., Perkin Trans. 2*, 1993, 799-805.
16. T. Yanai, D. P. Tew and N. C. Handy, *Chem. Phys. Lett.*, 2004, **393**, 51-57.
17. E. J. Blaesi, B. G. Fox and T. C. Brunold, *Biochemistry*, 2015, **54**, 2874-2884.
18. A. A. Fischer, N. Stracey, S. V. Lindeman, T. C. Brunold and A. T. Fiedler, *Inorg. Chem.*, 2016, **55**, 11839-11853.
19. S. Hirata and M. Head-Gordon, *Chem. Phys. Lett.*, 1999, **314**, 291-299.
20. S. Hirata and M. Head-Gordon, *Chem. Phys. Lett.*, 1999, **302**, 375-382.